A 4th order accurate P-SV wave staggered grid finite difference algorithm with variable grid size and VGR-stress imaging technique

J. P. Narayan and Sanjay Kumar

Department of Earthquake Engineering, Indian Institute of Technology, Roorkee, India

The implementation of VGR-stress imaging technique, as a free surface boundary condition, in a (2, 4) staggered grid P-SV wave finite difference (FD) algorithm with a variable size of a grid cell is presented in this paper. VGR is acronym for 'vertical grid-size reduction'. The qualitative and quantitative results confirmed that the effective thickness (ETH) of the first soil layer become less by one-half of the vertical size of a grid cell than the assigned thickness (ATH), if stress imaging technique is used as a free surface boundary condition. The results of various numerical experiments revealed that the stress imaging technique causes significant numerical dispersion of Rayleigh waves and the VGR-stress imaging technique is efficient enough to avoid the same. So, superiority associated with the VGR-stress imaging technique over the well stress imaging technique is that it avoids both the significant numerical dispersion of Rayleigh waves in homogeneous medium and the soil thickness discrepancy. The maximum grid spacing ratio (ratio of largest to smallest size of a grid cell) up to 6.0 did not affect the accuracy of FD algorithm with a variable size of a grid cell. In case of a variable size of a grid cell, the required computational memory and time for a particular basin-edge model was 6.43 and 16.62 times lesser than that required in case of uniform grid.

Keywords: P-SV wave finite difference algorithm, fourth order spatial accuracy, maximum grid spacing ratio, VGR-stress imaging technique, stability and grid dispersion

1. Introduction

The accuracy of finite difference (FD) method very much depends on the efficiency of the implemented boundary condition at the free-surface. The staggered grid FD method, proposed by Madariaga (1976), is one of the most useful numerical methods to simulate the ground motion characteristics (Virieux, 1984; 1986; Levander, 1988; Luo and Schuster, 1990; Graves, 1996; Pitarka, 1999; Ohminato and Chouet; 1997; Narayan 2001a, 2001b; Moczo et al., 2002; Narayan and Kumar, 2008). In the past, a free surface boundary con-

dition has been achieved using either the stress imaging technique (Levander, 1988; Graves, 1996; Gottschammer and Olsen, 2001) or the vacuum formulation (Boore, 1972; Zahradnik et al., 1993; Oprsal and Zahradnik, 2002). The well known stress imaging technique was first proposed by Levender (1988) in his P-SV wave 4th order spatially accurate staggered grid FD scheme. Graves (1996) gave details of how to compute the required particle-velocity components above the free surface for the stress imaging technique.

Incorporation of local site effects (particularly lateral geometrical variations and a very soft soil layer) in a simulation requires very dense grid FD mesh (Jastram and Tessmer, 1994; Moczo et al., 1996; Pitarka, 1999; Oprsal and Zahradnik, 2002; Narayan, 2005; Narayan and Ram, 2006; Narayan and Singh, 2006). For example, in case of a very soft surficial soil layer, very small size of a grid cell is required to avoid the numerical dispersion, which in turn causes over sampling in a region where the seismic wave velocity is very large. If uniform grid is used to discretise the model, the method becomes very computationally expensive and time-consuming. In order to avoid this, a variable size of a grid cell with continuous or discontinuous grid mesh has been used in the past. The discontinuous grid mesh has been used in only one direction and it has not been fully generalized for treating the discontinuous grids in all the directions (Jastram and Tessmer, 1994; Moczo et al., 1996; Aoi and Fujiwara, 1999; Hayashi et al., 2001; Wang and Schuster, 2001). We have used a continuous grid mesh with a variable size of a grid cell (Miyatake, 1980; Moczo, 1989; Oprsal and Zahradnik, 1999; Pitarka, 1999; Oprsal and Zahradnik, 2002; Narayan and Kumar, 2008).

Fourth order accurate FD scheme requires only 6 grid points per-shortest wavelength to avoid the significant numerical dispersion of body waves. Bohlen and Saenger (2006) reported the need of at least 17 grid points per shortest wavelength to avoid the significant numerical dispersion of Rayleigh waves in soft rock. The effect of position of the free surface, i.e. whether the normal or shear stress components coincide with the free surface level, was studied by Gottschammer and Olsen (2001) in the form of misfit between the analytical and FD solution. It was inferred that the cause of error (misfit) may be due to the numerical dispersion of Rayleigh waves. Kristek et al. (2002) reported delayed and earlier arrival of Rayleigh waves in a staggered grid with horizontal and vertical component of particle displacement at the free surface, respectively.

Rodrigue (1993) used smaller size of a grid cell in vertical direction near the free surface to avoid the numerical dispersion of Rayleigh wave. Similar numerical experiment was done by Kristek et al. (2002) just to show that stress imaging technique requires at least 10 grid points per-shortest wavelength in order to avoid any significant numerical dispersion of Rayleigh wave. But, the requirement of smaller time step will increase the computational time. In case of VGR-stress imaging technique, the required stress and displacement components above and below the free surface are computed explicitly and there is no need of reducing the time step in order to satisfy the stabil-

ity condition (Narayan and Kumar, 2008). Kristek et al. (2002) have also developed a technique known as adjusted FD (ADFD) approximations to obtain a stress free boundary condition to avoid the significant dispersion of Rayleigh waves. The ADFD technique does not require the reduction of value of time step. Another problem associated with the combination of staggered grid and stress imaging technique is the thickness discrepancy of first soil layer as was reported by Narayan and Kumar (2008) using a SH-wave FD algorithm. This thickness discrepancy causes apparent faster movement of the body wave multiples and larger value of predicted fundamental frequency of the soil deposit (Narayan and Kumar, 2008). The VGR-stress imaging technique is efficient enough to avoid the soil thickness discrepancy. But, whether such type of discrepancy will arise by using ADFD technique or not has not been studied.

So, in order to avoid the significant numerical dispersion of Rayleigh wave and the thickness discrepancy of the first soil layer in case of a P-SV wave simulation, we have developed a procedure for the implementation of the VGR-stress imaging technique (proposed by Narayan and Kumar (2008) for (2, 4) SH-wave staggered grid FD scheme) in a newly developed (2, 4) P-SV wave staggered grid FD algorithm. VGR is acronym for 'vertical grid-size reduction'. The VGR-stress imaging technique is based on the vertical grid-size reduction above the free surface during the explicit computation of the free surface boundary condition. So, there is no need of reducing the time step in order to satisfy the stability condition. In this paper, we have studied in detail the performance of VGR-stress imaging technique in avoiding the significant numerical dispersion of Rayleigh waves in a homogeneous half-space and soil thickness discrepancy. We have also conducted various numerical experiments to verify that the well known stress imaging technique (Levander, 1988; Graves, 1996) suffers from numerical dispersion of Rayleigh waves and the soil thickness discrepancy. The maximum grid spacing ratio, stability and grid dispersion are also studied. Numerical experiments are conducted to determine the saving of computational memory and time in case of a variable size of a grid cell.

Both the sponge boundary condition (Israeli and Orszag, 1981; Dablain, 1986) and the A1 absorbing boundary condition of Clayton and Engquist (1977), modified for the use with a variable size of a grid cell were implemented on the model edges to avoid the edge reflections, as was used by Kumar and Narayan (2008) for SH-wave. A time domain attenuation operator based on an approximate technique is used for the modeling of spatially varying visco-elastic media (Graves, 1996; Kumar and Narayan, 2008). Dominant frequency (f_0) in the middle of the desired frequency band was chosen as reference frequency. An attenuation operator (A) used in the simulation and applied at a grid point (i, l) for duration t, the time step, is given below,

$$A_{i,l} = \exp\left(-\frac{\pi f_0 \Delta t}{Q_{i,l}^s}\right)$$

where Q^s: the quality factor for S-wave is used since it is difficult to distinguish the P- and S-waves in the finite difference time domain calculations. Q^s was taken as 10% of the value of S-wave velocity at the grid nodes.

2. (2, 4) P-SV wave FD algorithm with variable size of a grid cell

The computer program developed is based on the second order temporal and fourth order spatial (2, 4) FD approximation of elastodynamic P-SV wave equations in the form of displacement-stress relations (Luo and Schuster, 1990; Ohminato and Chouet; 1997). In order to reduce the requirement of computational memory displacement-stress relation is used which requires stress components at only one time step in the memory where as in case of FD program based on velocity-stress relation requires stress components at two time steps in the memory.

2.1. (2, 4) FD approximation of P-SV wave equation

The elastodynamic wave equations for P-SV wave propagation in heterogeneous media is.

$$\rho \frac{\partial^2 U}{\partial t^2} = \frac{\partial \sigma_{xx}}{\partial x} + \frac{\partial \sigma_{xz}}{\partial z} \tag{1}$$

$$\rho \frac{\partial^2 W}{\partial t^2} = \frac{\partial \sigma_{xz}}{\partial x} + \frac{\partial \sigma_{zz}}{\partial z} \tag{2}$$

Stress-strain relationship is given below

$$\sigma_{xx} = (\lambda + 2\mu) \frac{\partial U}{\partial x} + \lambda \frac{\partial W}{\partial z} \tag{3}$$

$$\sigma_{zz} = (\lambda + 2\mu) \frac{\partial W}{\partial z} + \lambda \frac{\partial U}{\partial x} \tag{4}$$

$$\sigma_{xz} = \mu \left(\frac{\partial U}{\partial z} + \frac{\partial W}{\partial x} \right) \tag{5}$$

where U and W are the components of particle displacement in the horizontal and vertical directions. σ_{xx}, σ_{zz} and σ_{xz} are the stress components, ρ is density, λ and μ are the Lame's constants. $\frac{\partial}{\partial x}$, $\frac{\partial}{\partial z}$ and $\frac{\partial^2}{\partial t^2}$ are the differential operators.

Figure 1a shows the staggering technique, where normal stress components and the Lame's parameters are defined at the nodes. The shear stress component and the modulus of rigidity are defined at the centre of a grid cell.
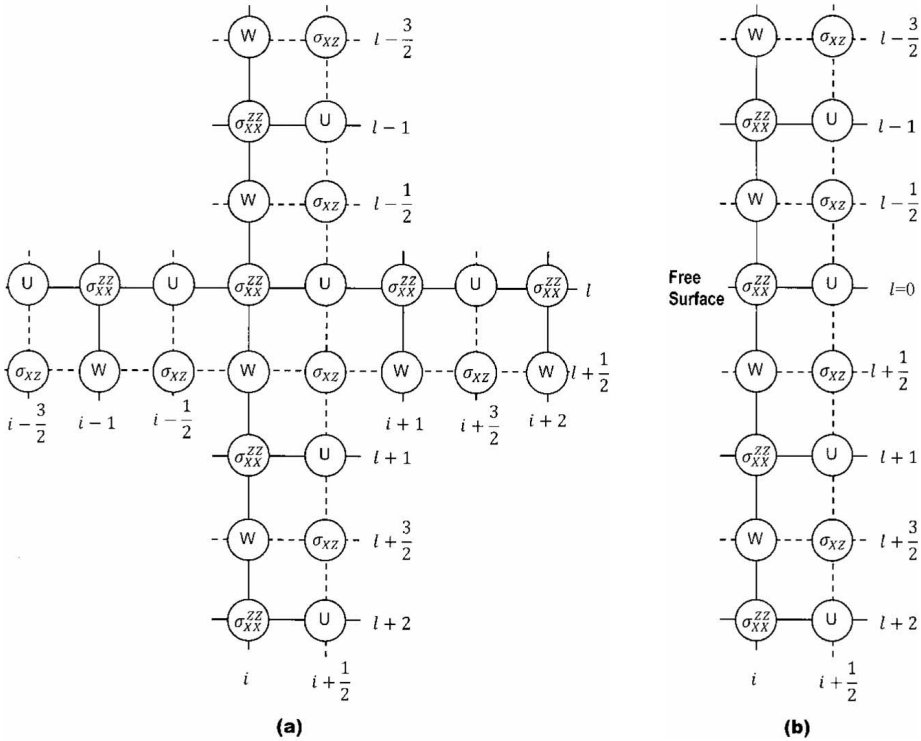
Figure 1a. Staggering technique for P-SV wave modeling with fourth order spatial accuracy. Particle displacement and density are defined the midway between two adjacent grid points in the horizontal and vertical directions. Normal stress components and Lame's parameters are defined at grid nodes and shear stress component and modulus of rigidity are defined at the centre of the grid cell; and **1b**. extended grid points above the free surface.

Horizontal and vertical components of the particle displacement and the density are defined at the midway between the two adjacent grid points in the horizontal and vertical directions, respectively. In equations (1) – (5), the time derivative was replaced by second order accurate central difference FD operator (Boore, 1972; Dablain, 1986) and the space derivatives were replaced by a fourth order staggered grid FD operator (Levander, 1988; Graves, 1996; Pitarka, 1999; Moczo et al., 2002).

$$U_{i+\frac{1}{2},l}^{n+1} = 2U_{i+\frac{1}{2},l}^{n} - U_{i+\frac{1}{2},l}^{n-1} + \frac{\Delta t^2}{\rho_{i+\frac{1}{2},l}} \left[\frac{a\{(\sigma_{xx})_{i+2,l}^{n} - (\sigma_{xx})_{i-1,l}^{n}\} + b\{(\sigma_{xx})_{i+1,l}^{n} - (\sigma_{xx})_{i,l}^{n}\}}{\Delta X_{i,l}} + \right.$$

$$\left. + \frac{a\{(\sigma_{xz})_{i+\frac{1}{2},l+\frac{3}{2}}^{n} - (\sigma_{xz})_{i+\frac{1}{2},l-\frac{3}{2}}^{n}\} + b\{(\sigma_{xz})_{i+\frac{1}{2},l+\frac{1}{2}}^{n} - (\sigma_{xz})_{i+\frac{1}{2},l-\frac{1}{2}}^{n}\}}{(\Delta Z_{i,l} + \Delta Z_{i,l-1})/2} \right] \qquad (6)$$

$$W_{i,l+\frac{1}{2}}^{n+1} = 2W_{i,l+\frac{1}{2}}^{n} - W_{i,l+\frac{1}{2}}^{n-1} +$$

$$+ \frac{\Delta t^2}{\rho_{i,l+\frac{1}{2}}} \left[\frac{a\{(\sigma_{xz})_{i+\frac{3}{2},l+\frac{1}{2}}^{n} - \{(\sigma_{xz})_{i-\frac{3}{2},l+\frac{1}{2}}^{n}\} + b\{(\sigma_{xz})_{i+\frac{1}{2},l+\frac{1}{2}}^{n} - \{(\sigma_{xz})_{i-\frac{1}{2},l}^{n}\}}{(\Delta X_{i,l} + \Delta X_{i-1,l})/2} + \right.$$

$$\left. + \frac{a\{(\sigma_{zz})_{i,l+2}^{n} - (\sigma_{zz})_{i,l-1}^{n}\} + b\{(\sigma_{zz})_{i,l+1}^{n} - (\sigma_{zz})_{i,l}^{n}\}}{\Delta Z_{i,l}} \right] \qquad (7)$$

$$(\sigma_{xx})_{i,l}^{n+1} = (\lambda + 2\mu)_{i,l} \left[\frac{a\left(U_{i+\frac{3}{2},l}^{n+1} - U_{i-\frac{3}{2},l}^{n+1}\right) + b\left(U_{i+\frac{1}{2},l}^{n+1} - U_{i-\frac{1}{2},l}^{n+1}\right)}{(\Delta X_{i,l} + \Delta X_{i-1,l})/2} \right] +$$

$$\lambda_{i,l} \left[\frac{a\left(W_{i,l+\frac{3}{2}}^{n+1} - W_{i,l-\frac{3}{2}}^{n+1}\right) + b\left(W_{i,l+\frac{1}{2}}^{n+1} - W_{i,l-\frac{1}{2}}^{n+1}\right)}{(\Delta Z_{i,l} + \Delta Z_{i,l-1})/2} \right] \qquad (8)$$

$$(\sigma_{zz})_{i,l}^{n+1} = (\lambda + 2\mu)_{i,l} \left[\frac{a\left(W_{i,l+\frac{3}{2}}^{n+1} - W_{i,l-\frac{3}{2}}^{n+1}\right) + b\left(W_{i,l+\frac{1}{2}}^{n+1} - W_{i,l-\frac{1}{2}}^{n+1}\right)}{(\Delta Z_{i,l} + \Delta Z_{i,l-1})/2} \right] +$$

$$+ \lambda_{i,l} \left[\frac{a\left(U_{i+\frac{3}{2},l}^{n+1} - U_{i-\frac{3}{2},l}^{n+1}\right) + b\left(U_{i+\frac{1}{2},l}^{n+1} - U_{i-\frac{1}{2},l}^{n+1}\right)}{(\Delta X_{i,l} + \Delta X_{i-1,l})/2} \right] \qquad (9)$$

$$(\sigma_{xz})_{i+\frac{1}{2},l+\frac{1}{2}}^{n+1} = \mu_{i+\frac{1}{2},l+\frac{1}{2}} \left[\frac{a\left(U_{i+\frac{1}{2},l+2}^{n+1} - U_{i+\frac{1}{2},l-1}^{n+1}\right) + b\left(U_{i+\frac{1}{2},l+1}^{n+1} - U_{i+\frac{1}{2},l}^{n+1}\right)}{\Delta Z_{i,l}} \right] +$$

$$+ \mu_{i+\frac{1}{2},l+\frac{1}{2}} \left[\frac{a\left(W_{i+2,l+\frac{1}{2}}^{n+1} - W_{i-1,l+\frac{1}{2}}^{n+1}\right) + b\left(W_{i+1,l+\frac{1}{2}}^{n+1} - W_{i,l+\frac{1}{2}}^{n+1}\right)}{\Delta X_{i,l}} \right] \qquad (10)$$

The values of constants a and b are –1/24 and 9/8, respectively. The super-script n refers to the time index and the subscript i and l are the spatial indices in the x and z directions, respectively. The time indices $n + 1$, n and $n − 1$ depict the updated, present and past wave fields, respectively. $\Delta X_{i,l}$ and $\Delta Z_{i,l}$ are the size of a grid cell at grid position i,l in x- and z-directions, respectively. The effective values of the modulus of rigidity, defined at the centre of grid have been obtained using a harmonic mean (Moczo et al., 2002).

$$\mu_{i+\frac{1}{2},l+\frac{1}{2}} = \left[\frac{1}{4}\left(\frac{1}{\mu_{i,l}} + \frac{1}{\mu_{i+1,l}} + \frac{1}{\mu_{i,l+1}} + \frac{1}{\mu_{i+1,l+1}} \right) \right]^{-1} \tag{11}$$

Similarly, effective values of density defined at the midway between the two adjacent grid points have been obtained using an arithmetic mean (Moczo et al., 2002).

$$\rho_{i+\frac{1}{2},l} = \frac{\rho_{i+1,l} + \rho_{i,l}}{2} \quad \text{and} \quad \rho_{i,l+\frac{1}{2}} = \frac{\rho_{i,l+1} + \rho_{i,l}}{2} \tag{12}$$

2.2. VGR – stress imaging technique

The medium parameters, displacement and stress components are not col-located in a staggered grid FD scheme (Figure 1a). In case of heterogeneous media, for example in vertical direction, the boundaries between two horizontal layers do not coincide with the grid points, since shear stress component is defined at the centre of a grid cell and horizontal and vertical components of the particle displacement are defined at the midway between two adjacent grid points. The computation of shear stress and displacement components require the shear modulus and density at the same point where these are defined. The shear modulus at the centre of a grid cell is obtained using equation (11) and density at the midway between the two adjacent grid points has been computed using equation (12). In a heterogeneous medium, the effective interface between layers will be half a grid spacing displaced from the level determined by grid points (where horizontal component of particle displacement is calculated).

We have defined the free surface collocated with grid nodes where horizontal component of the particle displacement is located (Figure 1b). It means the effective interface between the first soil layer and the vacuum/air will lay a half of the vertical grid spacing above the free surface level where the horizontal component of particle displacement is assigned. If the stress imaging is used as the free surface boundary condition then the effective thickness (ETH) of the first soil layer is lesser by one half of vertical grid-size than the assigned thickness (ATH) for the horizontal component of particle displacement. On the other hand, the ETH of the soil layer for the vertical component of particle

displacement will be the same as the ATH. This thickness discrepancy (ATH–ETH) of the first soil layer may cause considerable error in the computed fundamental frequency of the soil layer. Further, this thickness discrepancy may cause apparently faster movement of the body wave multiples.

To avoid the thickness discrepancy of the first soil layer and the significant numerical dispersion of Rayleigh wave in a homogeneous half-space, we have used the VGR-stress imaging technique, where vertical size of a grid cell above the free surface is reduced during the explicit computation of the free surface boundary condition. If, the vertical size of a grid cell above the free surface tends to zero, then virtually, the interface between the first soil layer and the vacuum/air coincides with the free surface. So, effectively, we get the ETH of the first soil layer same as the ATH. In the following paragraphs, details of how to compute the required displacement and stress components above the free surface with the reduced vertical size of a grid cell above the free surface is given.

To compute the particle displacement at the free surface and one-half as well as one grid below the free surface, the stress components σ_{zz}, σ_{xx} and σ_{xz} will be required above the free surface (Figure 1b). To fulfill this requirement, two grid nodes are extended in the vertical direction above the free surface. The stress components σ_{zz} and σ_{xz} above the free surface are obtained using the well known stress imaging technique (Levander, 1988; Graves, 1996)

$$(\sigma_{zz})_{i,\,l=0} = 0 \tag{13}$$

$$(\sigma_{zz})_{i,\,l-1} = -(\sigma_{zz})_{i,\,l+1} \tag{14}$$

$$(\sigma_{xz})_{i+\frac{1}{2},\,l-\frac{1}{2}} = -(\sigma_{xz})_{i+\frac{1}{2},\,l+\frac{1}{2}} \tag{15}$$

$$(\sigma_{xz})_{i+\frac{1}{2},\,l-\frac{3}{2}} = -(\sigma_{xz})_{i+\frac{1}{2},\,l+\frac{3}{2}} \tag{16}$$

In order to introduce the effects of reduction of vertical size of a grid cell above the free surface, let us assume that vertical size of a grid cell above the free surface is reduced by a factor K as compared to the vertical size of a grid cell just below the free surface (where $K = \dfrac{\Delta Z \ below \ the \ free \ surface}{\Delta Z \ above \ the \ free \ surface}$ is the vertical size of a grid cell reduction factor (VGRF)). During the computation of normal stresses σ_{xx} and σ_{zz} at $l = 0$ and $l + 1$, just at the free surface and one grid size below the free surface, the vertical component of particle displacement $W_{i,\,l-\frac{1}{2}}$ and $W_{i,\,l-\frac{3}{2}}$ will be required above the free surface (Figure 1b). It was assumed that the Lame's parameters are constant across the free surface. First, vertical component of particle displacement $W_{i,\,l-\frac{1}{2}}$ was obtained using

equations (9) and (13). We have used second order approximation of equation (9) as suggested by Graves (1996).

$$(\sigma_{zz})^{n+1}_{i,\,l=0} = (\lambda + 2\mu)_{i,\,l=0}\left[\frac{\partial w}{\partial z}\right] + (\lambda)_{i,\,l=0}\left[\frac{\partial u}{\partial x}\right] = 0$$

$$(\lambda + 2\mu)_{i,\,l=0}\left[\frac{W^{n+1}_{i,\,l+\frac{1}{2}} - W^{n+1}_{i,\,l-\frac{1}{2}}}{\frac{\Delta Z_{i,\,l-1} + \Delta Z_{i,\,l}}{2}}\right] = -(\lambda)_{i,\,l=0}\left[\frac{U^{n+1}_{i+\frac{1}{2},\,l=0} - U^{n+1}_{i-\frac{1}{2},\,l=0}}{\frac{\Delta X_{i-1,\,l=0} + \Delta X_{i,\,l=0}}{2}}\right]$$

$$W^{n+1}_{i,\,l-\frac{1}{2}} = W^{n+1}_{i,\,l+\frac{1}{2}} + \left(\frac{\lambda}{\lambda + 2\mu}\right)_{i,\,l=0}\frac{\Delta Z_{i,\,l-1} + \Delta Z_{i,\,l}}{\Delta X_{i-1,\,l=0} + \Delta X_{i,\,l=0}}\left[U^{n+1}_{i+\frac{1}{2},\,l=0} - U^{n+1}_{i-\frac{1}{2},\,l=0}\right]$$

If the vertical size of a grid cell above the free surface is K times smaller than below the free surface ($\Delta Z_{i,\,l-1} = \Delta Z_{i,\,l+1}/K$), then

$$W^{n+1}_{i,\,l-\frac{1}{2}} = W^{n+1}_{i,\,l+\frac{1}{2}} + \left(\frac{\lambda}{\lambda + 2\mu}\right)_{i,\,l=0}\frac{\Delta Z_{i,\,l}}{\Delta X_{i-1,\,l=0} + \Delta X_{i,\,l=0}}\left(\frac{1}{K} + 1\right)\left[U^{n+1}_{i+\frac{1}{2},\,l=0} - U^{n+1}_{i-\frac{1}{2},\,l=0}\right] \quad (17)$$

During the computation of shear stress σ_{xz} at $l + 1/2$ just half grid size below the free surface, the horizontal component of particle displacement $U_{i+\frac{1}{2},\,l-1}$ will be required one grid point above the free surface (Figure 1b). The horizontal component of particle displacement $U_{i+\frac{1}{2},\,l-1}$ was obtained using equations (10) and (15).

$$U^{n+1}_{i+\frac{1}{2},\,l-1} = U^{n+1}_{i+\frac{1}{2},\,l=0} + \frac{\Delta Z_{i,\,l=0}}{K\Delta X_{i,\,l=0}}\left[W^{n+1}_{i+1,\,l-\frac{1}{2}} - W^{n+1}_{i,\,l-\frac{1}{2}} + W^{n+1}_{i+1,\,l+\frac{1}{2}} - W^{n+1}_{i,\,l+\frac{1}{2}}\right] \quad (18)$$

Similarly, vertical component of particle displacement $W^{n+1}_{i,\,l-\frac{3}{2}}$ above the free surface was obtained using equations (9), (14), (17) and (18).

$$W^{n+1}_{i,\,l-\frac{3}{2}} = W^{n+1}_{i,\,l-\frac{1}{2}} +$$

$$\left(\frac{\lambda}{\lambda + 2\mu}\right)_{i,\,l=0}\frac{2\Delta Z_{i,\,l}}{K(\Delta X_{i-1,\,l} + \Delta X_{i,\,l})}\left[U^{n+1}_{i+\frac{1}{2},\,l-1} - U^{n+1}_{i-\frac{1}{2},\,l-1} + U^{n+1}_{i+\frac{1}{2},\,l+1} - U^{n+1}_{i-\frac{1}{2},\,l+1}\right] \quad (19)$$

Further, it was assumed that in the VGR-stress imaging technique, the stress components at $l + 1/2$, $l + 1$ or $l + 3/2$ first linearly reduces to zero up to the free surface and then linearly increases up to $l - 1/2$, $l - 1$ or $l - 3/2$ above the free surface. It means, under this assumption, if the size of a grid cell

above the free surface is reduced by K then the stress components above the free surface respectively at $l - 1/2$, $l - 1$ or $l - 3/2$ will be.

$$\frac{(\sigma_{xz})_{i+\frac{1}{2},l-\frac{1}{2}}}{K} \quad (20)$$

$$\frac{(\sigma_{zz})_{i,l-1}}{K} \quad (21)$$

$$\frac{(\sigma_{xz})_{i+\frac{1}{2},l-\frac{3}{2}}}{K} \quad (22)$$

The required displacement components above the free surface to implement the free surface boundary condition using the stress imaging technique can be obtained using $K = 1$ in equations (17), (18) and (19).

3. Validation of (2, 4) P-SV wave FD scheme

3.1. Numerical grid dispersion and stability

It is well documented that at least 6 grid points per-shortest wavelength are required in case of a fourth order accuracy to avoid significant numerical dispersion of body waves (Levander, 1988; Moczo et. al., 2000; Narayan and Kumar, 2008). Although, there is no need to study the numerical dispersion but just to verify the performance of new FD algorithm, seismic response of a homogeneous model were computed using different number of grid points per-shortest wavelength. The P-wave and S-wave velocities, quality factor and density for the homogeneous model were taken as 3 117.7 m s^{-1}, 1 800 m s^{-1}, 180 and 2.5 g cm^{-3}, respectively. Ricker wavelet with 1.0 Hz dominant frequency and upper frequency limit of 3.0 Hz was used as an excitation function. The model was discretised using a square grid of size 50 m, 100 m, 120 m and 150 m, with effectively 12.0, 6.0, 5.0 and 4.0 grid points per-shortest wavelength, respectively. Seismic responses were computed at an epicentral distance of 24.0 km using source at a focal depth of 12.0 km. Seismic response computed using 12 grid points per-shortest wavelength is used as a reference one assuming that it may be numerical dispersion free for a distance travelled equivalent to 15 dominant wavelength. Figure 2 shows the comparison of computed seismic response using 4, 5 and 6 grid points per-shortest wavelength (dotted line) with the reference one (solid line). P-wave, SV-wave converted in to P-wave and SV-wave are the first, second and third arrivals, respectively. Analysis of Figure 2 reveals that SV-wave converted P-wave and SV-wave have suffered significant dispersion in cases where there was only 4 and 5 grid point per-shortest wavelength. But, there is only minor numerical dispersion in FD response when there was 6 grid point per-shortest wavelength. Numerical dispersion of P-wave is all most negligible in responses where there was 5–6 grid point per-shortest wavelength. It can be inferred that numerical dispersion
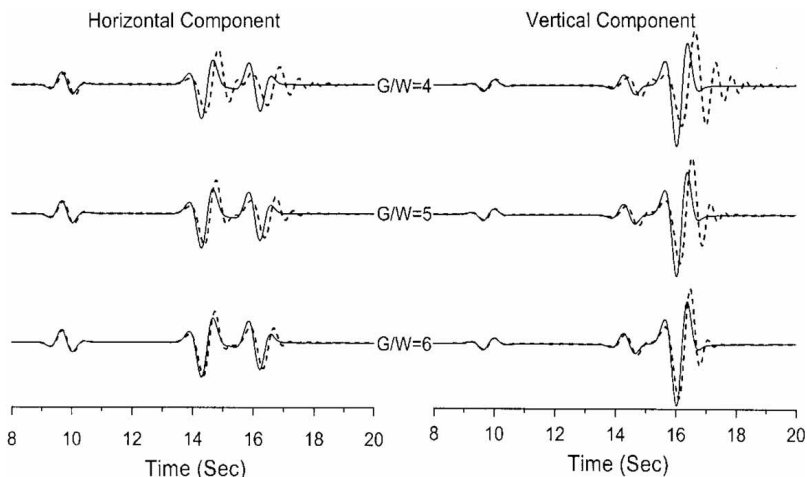
Figure 2. Comparison of computed responses of a homogeneous half-space model using different number of grid points per shortest wavelength (G/W) with the response computed using 12 grid points per-shorted wavelength.

may be negligible for a distance travelled equivalent to 10–12 dominant wavelength using 6 grid points per-shorted wavelength.

The stability condition for this new (2, 4) P-SV wave FD algorithm with variable size of a grid cell was obtained based on various iterative numerical experiments i.e. taking different time steps Δt for the simulation and then analyzing whether error increases with the simulation time step (Δt was varied in a very small step near the upper limit of the stability). Models with large velocity contrast (having both the lateral and vertical variations) and grid spacing ratio were considered for the numerical experiments. It was finally concluded that the scheme is stable for both the homogeneous and heterogeneous models, if the following stability condition is locally satisfied.

$$\frac{V_P \Delta t}{\min(\Delta x, \Delta z)} \le 0.71 \tag{23}$$

where V_P is the P-wave velocity. x and z are the grid spacing in the horizontal and vertical directions, respectively. Moczo et al. (2000) have given a stability condition exclusively for P- and S-waves with fourth order spatial accuracy for a homogeneous medium.

$$\frac{V \Delta t}{\Delta x \ or \ \Delta z} \le \frac{6}{7\sqrt{2}} \tag{24}$$

3.2. Maximum grid spacing ratio

Simulation of a model containing a lateral geometrical variations or a very soft soil with uniform grid requires very large computational memory and

time. In order to reduce the same, we have used a continuous grid mesh with a variable size of a grid cell (Miyatake, 1980; Moczo, 1989; Oprsal and Zahradnik, 1999; Pitarka, 1999; Oprsal and Zahradnik, 2002; Narayan, 2005; Narayan and Ram, 2006). Two additional grid cells were created to store the values of the size of a grid cell since a variable size of a grid cell FD scheme requires the information regarding the size of a grid cell in both the directions at each node for the computation of spatial derivatives.

To find out the maximum grid spacing ratio (ratio of largest to smallest size of a grid cell) up to which (2, 4) P-SV wave algorithm is accurate, the responses of same homogeneous model (21.1 km × 13.8 km) were computed. Model was discretised with larger size of a grid cell as 100 m and different smaller size of a grid cell as 25 m, 20 m, 16.66 m, 16.0 m and 15.0 m. So, we have larger to smaller grid spacing ratio as 1:4, 1:5, 1:6, 1:6.25 and 1:6.66. The horizontal dimension of the grid from left edge of the model was 100 m up to 9.0 km and thereafter variable (25 m, 20 m, 16.67 m, 16.0 m and 15.0 m). In the vertical direction, the size of a grid cell was variable (25 m, 20 m, 16.67 m, 16.0 m and 15.0 m) up to a depth of 4.8 km and 100 m thereafter. Seismic responses were computed at 13.6 km epicentral distance using source at a focal
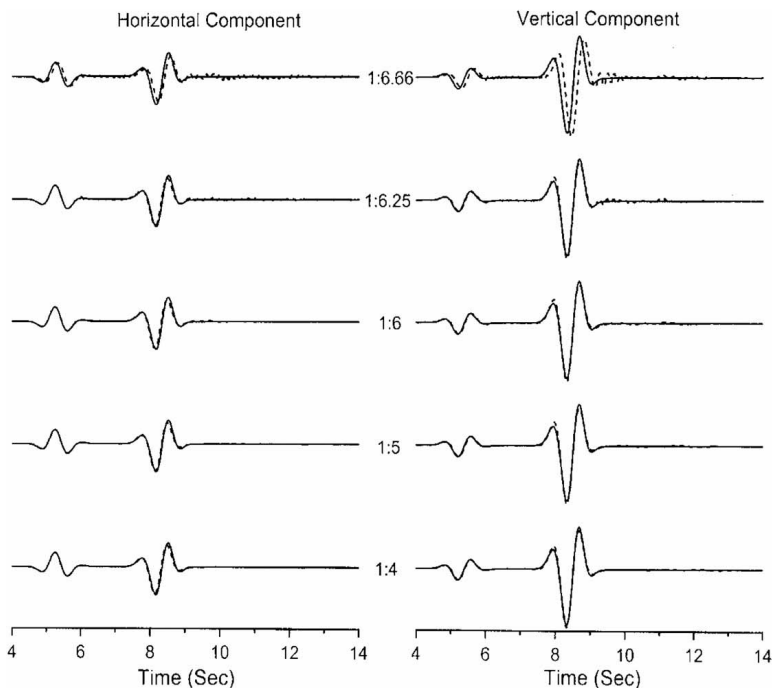

Figure 3. Comparison of computed responses of a homogeneous half-space model using different grid spacing ratio with the response computed using uniform grid.

depth of 8.8 km. The seismic response using uniform grid size of 100 m was also computed for the comparison. Figure 3 shows a comparison of computed responses using different grid spacing ratio (dotted line) with the response computed using uniform grid (solid line). It seems that in case of grid spacing ratio ≥ 6.25, a high frequency noised has been generated. Further, there is numerical dispersion in response computed using grid spacing ratio equal to 6.66. A good resemblance of responses for grid spacing ratios up to 6.0 with the response computed using uniform grid reveals that the maximum grid spacing ratio up to of the order of 6.0 can be used.

4. Performance of VGR-stress imaging technique

4.1. Soil thickness discrepancy

We have conducted numerical experiments to quantify the soil thickness discrepancy associated with the stress imaging technique as well as to show the effectiveness of the VGR-stress imaging technique in avoiding the same. Seismic response of a model with a soft soil layer over the half space was computed using different VGRF. The P-wave & S-wave velocities and densities were taken as 1,200 m $\cdot$ s^{-1}, 360.0 m $\cdot$ s^{-1} and 2.0 g $\cdot$ cm^{-3} for soil and 3 117.7 m $\cdot$ s^{-1}, 1 800.0 m $\cdot$ s^{-1} and 2.5 g $\cdot$ cm^{-3} for half-space. During the discretisation of the model, the horizontal dimension of the grid from left to right was 20 m and in vertical direction it was 20 m up to depth of 0.5 km and 100 m thereafter. Seismic responses of the model with soil thickness 200 m were computed at an epicentral distance of 6.0 km using a point source at a depth of 6.5 km. A comparison of seismic response with VGRF 1.0, 2.0, 4.0 and ∞ (∞ means 10^7; very
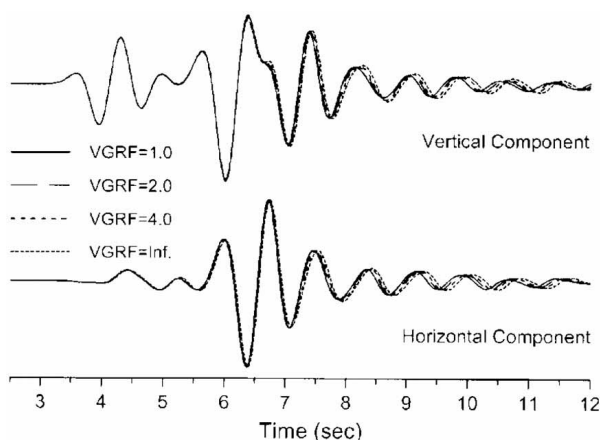
Figure 4. Comparison of computed FD response of a soil layer using stress imaging technique (VGRF=1) VGR-stress imaging technique with different VGRF.

large value) is shown in Figure 4. There is effect of used VGRF values on the arrival times of body waves and multiples. There is no change of arrival times of body waves in the vertical component since it is defined at one half of the size of a grid cell below the free surface. The multiples are moving faster in both the components of particle displacement when VGRF is smaller (note VGRF = 1.0 is equivalent to the use of the stress imaging technique). The multiples are moving faster in the vertical component also due to the faster movement of multiples in the horizontal component. For example, the multiples shown with solid line in Figure 4 is the fastest one, since in this case ETH of soil layer is 190 m (ATH – ETH = 10.0 m). The amplitude of multiples are unaffected by the used VGRF values. Analysis of Figure 4 confirms that the thickness discrepancy occurs for the first soil layer if stress imaging technique is used as the free surface boundary condition in case of horizontal component for the used discretisation scheme.

In order to show the above conclusion in a quantitative way and to quantify the error caused by the stress imaging technique, 1D seismic response of the same soil layer having thickness 180 m and different VGRF were computed using a source dominated by P-wave (P-wave dominated source was generated by using only normal stresses as source excitation function). The resonance frequency of soil for P-wave corresponding to different VGRF were computed using the ratio of spectra of vertical component computed with and

(a)

(b)
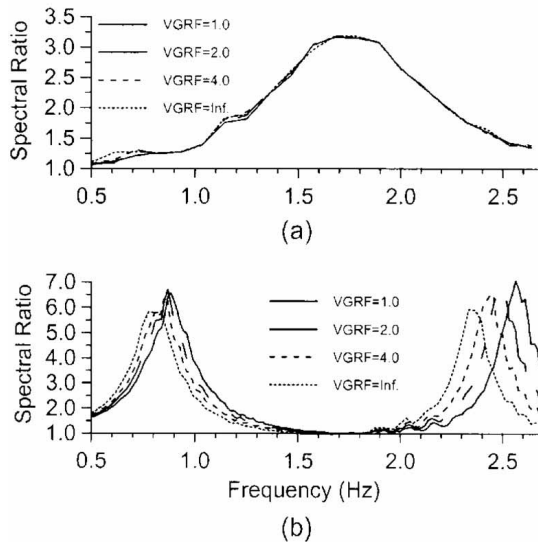
Figure 5. A comparison of variation of fundamental frequency and higher modes of resonance frequency of soil layer with VGRF in case of source dominated by P-wave (using vertical component) and S-wave (using horizontal component), respectively. (Note: considered thickness of soil in Figures 5a and 5b were 180 m and 120m, respectively).

without soil layer. Response in vertical component was used since amplitude in horizontal component was negligible. Figure 5a shows that there is no change in resonance frequency of soil with VGRF used since there is no soil thickness discrepancy in case of vertical component. The spectral ratio is not smooth due to presence of SV-wave in the computed response.

Table 1. A comparison of fundamental resonance frequency computed analytically using relation $F_{0ATH} = V_S/4(ATH)$ and obtained numerically for different VGRF and the % error.

F_{0ATH} (Hz)	VGFR = ∞		VGRF = 4		VGRF = 2		VGRF = 1	
	F_{0FD} (Hz)	% error	F_{0FD} (Hz)	% error	F_{0FD} (Hz)	% error	F_{0FD} (Hz)	% error
0.75	0.78	4.0	0.84	12.0	0.86	14.6	0.88	17.3

In the next numerical experiment, we computed 1D seismic response of the same soil layer with thickness 120 m and different VGRF using S-wave dominated source (source generated using shear stress '$\sigma_{x,z}$' as source excitation function). The resonance frequencies (fundamental and higher modes) of the soil layer using horizontal component were computed for different VGRF. Figure 5b shows that there is change in the resonance frequency of soil layer with VGRF used. The resonance frequency is increasing with the decrease of VGRF. A comparison of the empirically computed resonance frequency F_{0ATH} using assigned thickness (ATH) ($F_{0ATH} = V_S/(4 \cdot ATH)$) with the numerically obtained resonance frequency F_{0FD} and the % error for different VGRF is given in Table 1. The error between F_{0ATH} and F_{0FD} is decreasing with increase of VGRF. Maximum % error of the order of 17.3 % was obtained in case of the stress imaging technique (VGRF = 1.0) and minimum of the order of 4.0 % in case of the VGR-stress imaging technique (VGRF = 10^7). Theoretically, error should be 0.0 % for VGRF = 10^7. The observed error may be due to the resonance of P-wave at higher frequency. On the basis of analysis of Table 1, we can infer that the virtual reduction of the size of a grid cell above the free surface is almost linearly proportional to the used VGRF. The results support the conclusion in a quantitative way that the stress imaging technique suffers with the soil thickness discrepancy. The effective thickness of first soil layer becomes less by one half of the vertical size of a grid cell if stress imaging technique is used as a free surface boundary condition and the VGR-stress imaging technique is efficient enough to avoid the same (Narayan and Kumar, 2008).

4.2. Numerical dispersion of body wave propagating along the free surface

In order to study the performance of the VGR-stress imaging technique in avoiding the numerical dispersion of body wave propagation along the free

surface, we have first computed the response of a homogeneous half-space model using both stress imaging technique and VGR-stress imaging technique, keeping source at 6.0 km depth. The model parameters used during the simulation were the same as used earlier for the homogeneous half-space model. Responses were computed at five epicentral distances (14.0 km, 16.0 km, 18.0 km, 20.0 km and 22.0 km). Figure 6a shows the comparison of computed responses using the VGR-stress imaging technique (solid line) and the stress imaging technique (dotted line). Figure 6a clearly depicts P-wave as first arrival, evanescent P-wave caused by the critically incident SV-wave and propagating along the free surface as a second arrival and SV-wave as a third arrival. Rayleigh waves have not been generated for the source-receiver geometry and spectral content of the source-time function used in our computations. There is excellent matching of arrival times of evanescent P-wave propagating
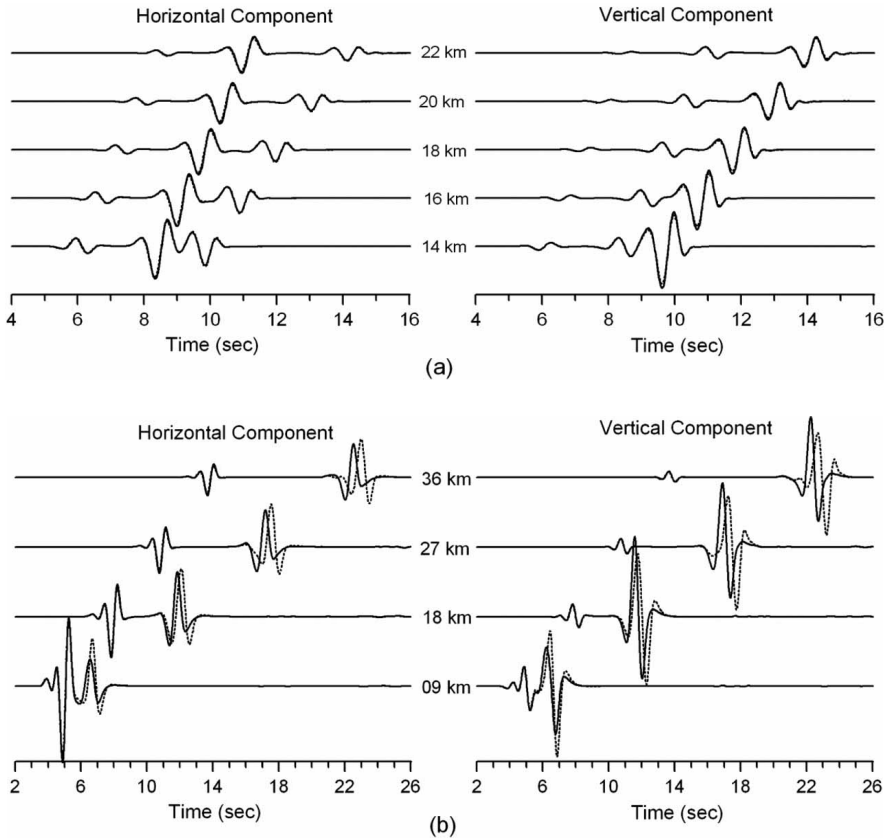

Figures 6a and 6b. Comparison of computed FD responses using stress imaging technique (dotted line) and VGR-stress imaging technique (solid line) at different epicentral distances using a deep source and a shallow source, respectively.

along the free surface in both the cases. We conclude that there is no numerical dispersion of body waves propagating along the free surface in case of stress imaging technique.

4.3. Numerical dispersion of Rayleigh wave

In order to show the efficacy of VGR-stress imaging technique to avoid the significant numerical dispersion of R-wave, seismic responses of a homogeneous half-space model were computed using both the stress imaging technique and the VGR-stress imaging technique. Response was computed at four epicentral distances 9.0 km, 18.0 km, 27.0 km and 36.0 km using source at a focal depth of 2.0 km. Figure 6b shows the comparison of computed responses using the stress imaging technique (dotted line) and the VGR-stress imaging technique (solid line). The first arrival in the response is the P-wave whose amplitude is very small compared to the other two seismic phases. The P-wave is only visible in trace recorded at an epicentral distance of 9 km. The second arrival is the evanescent P-wave caused by the SV-wave incident at the free surface at critical angle. The evanescent P-wave is propagating along the free surface. The third arrival is the Rayleigh wave caused by mainly incident SV-wave since source was dominated by SV-wave. The arrival time of evanescent P-wave is same at different epicentral distances in both the stress imaging technique and the VGR-stress imaging technique. There is dissimilarity in arrival time of peak amplitude Rayleigh wave (third arrival). The arrival time of peak amplitude Rayleigh wave in case of stress imaging technique (dotted line) is greater than that in case of VGR-stress imaging technique (solid line) and this difference in arrival time is increasing with the distance travelled. So, it can be inferred that the increase of difference in arrival time of peak amplitude Rayleigh wave with the distance travelled may be due to numerical dispersion of Rayleigh wave in the computed response using stress imaging technique.

In order to verify that there is no significant numerical dispersion of Rayleigh wave in the case of VGR-stress imaging technique, seismic responses were computed using different VGRF values. Figure 7a shows the response computed at 27 km epicentral distance using different VGRF. Again, there is no effect of VGRF on the arrival time of the evanescent P-wave. But, the travel time of peak amplitude Rayleigh is highly affected by the value of VGRF used. There is reduction of arrival time (dispersion) of peak amplitude Rayleigh wave with the increase of VGRF. So, it can be inferred that delay in arrival time of peak amplitude Rayleigh wave is largest in case of response computed using stress imaging technique (VGRF = 1) and it is theoretically negligible in case of VGRF = ∞ (10^7). The decrease in delay of arrival time of peak amplitude Rayleigh wave is proportional to the VGRF used. The numerical dispersion is also causing change of wavelet shape.
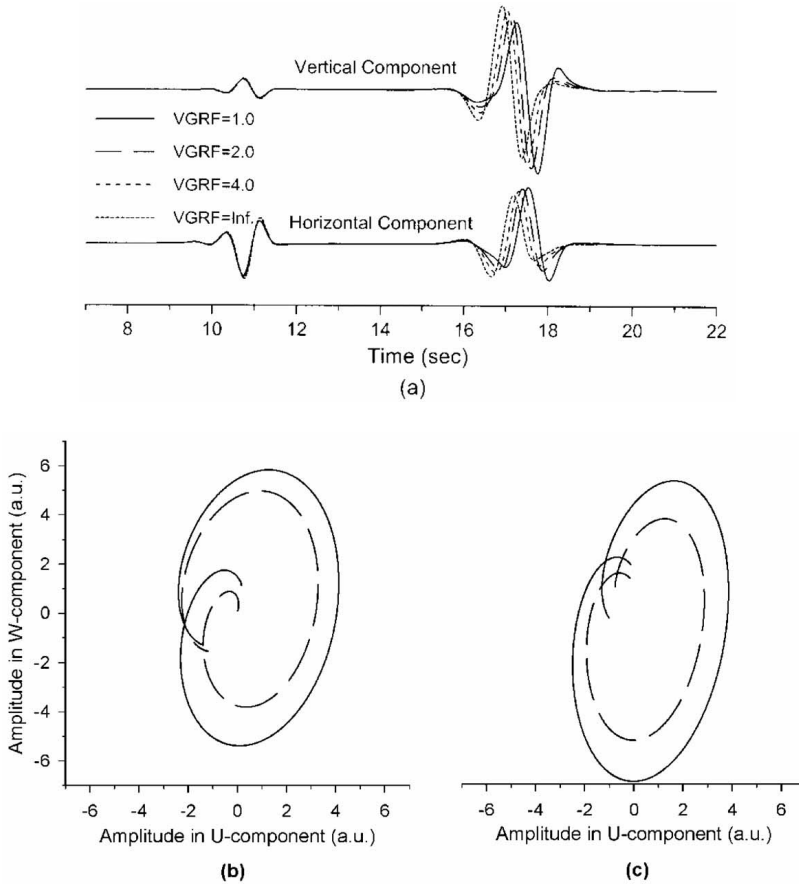
Figures 7a-7c. Comparison of computed response at an epicentral distance of 27.0 km using different VGRF; and shape of the particle motion trajectory at epicentral distances of 18 km (solid line) and 36 km (dotted line) using (b) stress imaging technique) and (c) VGR-stress imaging technique for VGRF = 10^7 (Note: a.u. means arbitrary unit).

In order to further confirm that VGR-stress imaging technique does not cause significant numerical dispersion of Rayleigh wave, seismic responses computed at epicentral distances of 18.0 km and 36.0 km using stress imaging technique (VGRF = 1) and VGR-stress imaging technique (VGRF = 10^7) were used to plot the particle motion trajectory during Rayleigh wave propagation. The seismic response in time windows of 10–14 sec and 22–26 sec corresponding to epicentral distances of 18 km and 36 km were used to plot the elliptical path of the particle motion. Figures 7b and c depict the comparative plot of the particle motion trajectory at epicentral distance of 18 km (solid line) and 36 km (dotted line) corresponding to stress imaging technique and VGR-stress imaging technique, respectively. The shape of the particle motion trajectory in

case of stress imaging technique is not preserved since the later part of trajectory corresponding to 36 km epicentral distance (dotted line) is touching to the trajectory corresponding to 18 km epicentral distance (solid line). This may be due to the increased amplitude of Rayleigh wave in later part of the wavelet and change of wavelet shape due to the numerical dispersion. On the other hand, the preserved shape of the particle motion trajectory with the distance travelled in case of the VGR-stress imaging technique (Figure 7c) further confirms that VGR-tress imaging technique is free from any significant numerical dispersion of Rayleigh wave.

5. Saving of computational time and memory

In order to compare the requirements of computational time and memory between the FD numerical schemes using a variable and fixed grid size step, respectively, we calculated synthetic seismograms for a shallow sedimentary basin (Figure 8a).

The parameters for the soil in basin and the bedrock were the same as used earlier. The size of considered basin-edge model was 14.0 km × 13.14 km and the basin-edge slope was 90°. The basin-edge was at a distance of 8.0 km from the left edge of the model. The soil thickness in the basin was taken as 140 m and its right edge was extending infinitely. Source was kept at a depth of 9.14 km and at a distance of 4.0 km from the left edge of the model. The width of sponge zone was 2.0 km in both the homogeneous and variable grid size models, which is essential to avoid the edge reflections. In case of uniform grid-size mesh, the size of a grid cell was taken as 20 m in both the direction. In case of a variable grid-size mesh, horizontal size of a grid cell was 100 m up to 8.0 km from left edge of the model, it was 20 m between 8.0 km and 12 km and 100 m thereafter. In the vertical direction, the size of a grid cell was 20 m up to a depth of 140 m and 100 m thereafter. The seismic response with time step 0.004 s was computed on a HP-Workstation (xw6000 model) with 4.0 GB RAM and 2.8 GHz processor's speed for a duration of 35 seconds. Seismic responses were computed at 30 equidistant (100 m apart) receiver points extending from 100 m left of edge to 2.8 km inside the basin. Figures 8 b & c show the horizontal components of computed seismic responses of basin-edge model using uniform grid and a variable size of a grid cell, respectively.

The required numbers of grid points in the x- and z-directions in both the discretisation schemes are given in Table 2. The number of numerical cells required to keep the different parameters in the computational memory in case of the uniform grid and variable size of a grid cell were 12 and 14, respectively. Two extra numerical cells were required in case of variable size of a grid cell to keep the information regarding the size of a grid cell in two directions. The common 12 numerical cells were one each for two Lame's parameters, density, velocity, quality factor, three stress components and two components of dis-

placement at two time steps. The total number of required nodes and the computational times in both the discretisation schemes are also given in Table 2. The analysis of Table 2 reflects 9.43 times saving of computational memory
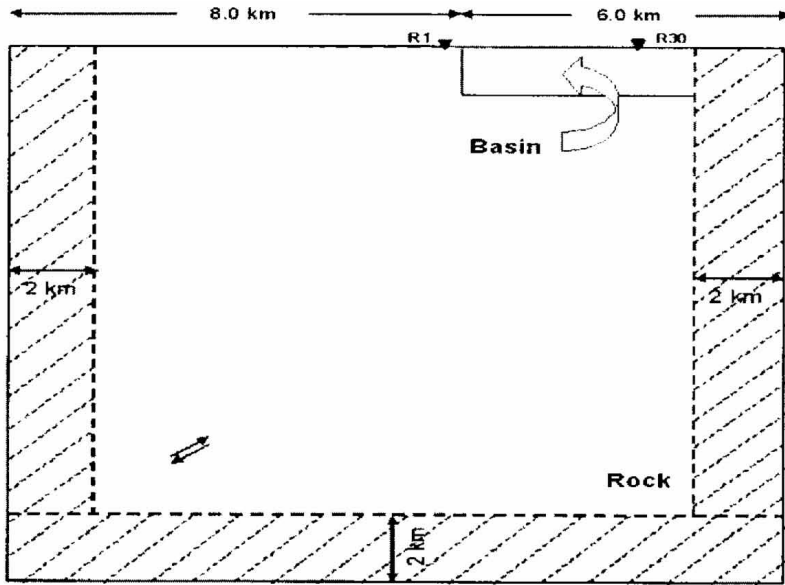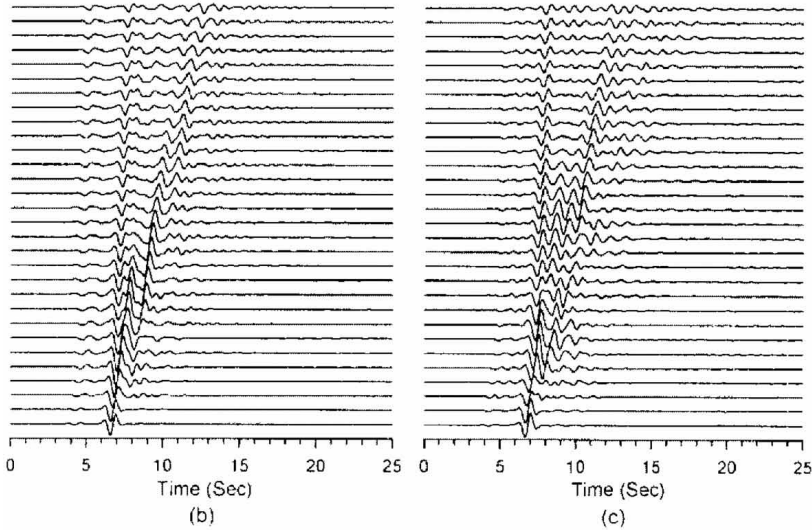
Figures 8a to 8c. shows the basin-edge model and b & c show the horizontal components of the responses computed using uniform grid and a variable size of a grid cell.

and 16.6 times saving of computational time in case of variable size of a grid cell as compared with the uniform grid.

Table 2. shows the number of grid points needed in the x-direction (IX) and z-direction (JZ) to discretise the basin-edge model with uniform size of a grid cell and variable size of a grid cell. N_H and N_V are the number of grid nodes and T_H and T_V are the computational time for uniform the size of a grid cell and variable the size of a grid cell discretisation schemes, respectively.

Uniform size of a grid cell				Variable size of a grid cell				Ratio	
No. of grids		No. of nodes	Comp. time T_H (sec)	No. of grids		No. of nodes	Comp. time T_V (sec)	N_H/N_V	T_H/T_V
IX	JZ	$N_H = IX \cdot JZ \cdot 12$		IX	JZ	$N_V = IX \cdot JZ \cdot 14$			
700	660	5 544 000	20.77	300	140	588 000	1.25	9.43	16.62

6. Discussion and conclusions

A new (2, 4) staggered grid FD algorithm with variable size of a grid cell and VGR-stress imaging technique as the free surface boundary condition is presented for the simulation of P-SV wave propagation in a heterogeneous medium. The qualitative and quantitative results of numerical experiments confirmed that FD algorithm with stress imaging technique as the free surface boundary condition suffers from soil thickness discrepancy while VGR-stress imaging technique is not affected by this effect. Similar conclusion was also drawn by Narayan and Kumar (2008) using (2,4) staggered grid SH-wave FD algorithm. The analysis of simulated results revealed that maximum grid spacing ratio of the order of 6.0 can be used for numerical simulation. In case of a variable size of a grid cell, the required computational memory and time for a particular basin-edge model was 6.43 and 16.62 times lesser than that required in case of uniform grid.

The analysis of simulated results confirmed that the use of stress imaging technique as a free surface boundary condition causes significant numerical dispersion of Rayleigh waves. Similar conclusion was also drawn by Rodrigues (1993) and Kristek et al. (2002). Based on various simulated results, we conclude that VGR-stress imaging technique is efficient enough to avoid significant numerical dispersion of Rayleigh wave, arising due to use of image of stress components across the free surface. The preserved shape of the elliptical particle motion trajectory with the travelled distance further supports that the VGR-stress imaging technique does not suffer with the significant numerical dispersion of Rayleigh wave. Further, in VGR-stress imaging technique required stress and displacement components above and below the free surface are computed explicitly so there is no need of reducing the time step in order to satisfy the stability condition. Finally, we conclude that the VGR-stress imaging technique is better than the well known stress imaging technique (Levander, 1988; Graves, 1996).

References

Aoi, S. and Fujiwara, H. (1999): 3D finite difference method using discontinuous grids, *Bull. Seism. Soc. Am.,* **89**, 918–930.

Bohlen, T. and Saenger, E. H. (2006): Accuracy of heterogeneous staggered grid finite difference modelling of Rayleigh waves, *Geophysics*, **71**, T109–T115.

Boore, D. M. (1972): Finite difference methods for seismic wave propagation in heterogeneous materials, In *Methods in Computational Physics*, edited by B. A. Bolt, **11**, Academic Press Inc., New York, 1-37.

Clayton, R. W. and Engquist, B. (1977): Absorbing boundary conditions for acoustic and elastic wave equations, *Bull. Seism. Soc. Am.*, **67**, 1529–1540.

Dablain, M. A. (1986): The application of high-order differencing to the scalar wave equation, *Geophysics*, **51**, 54–66.

Gottschammer, E. and Olsen, K. B. (2001): Accuracy of the explicit planar free surface boundary condition implemented in a fourth-order staggered-grid velocity-stress finite-difference scheme, *Bull. Seism. Soc. Am.*, **91**, 617–623.

Graves, R. W. (1996): Simulating seismic wave propagation in 3-D elastic media using staggered grid finite difference, *Bull. Seism. Soc. Am.*, **86**, 1091–1107.

Hayashi, K., Burns, D. R. and Toksoz, M. N. (2001): Discontinuous grid finite difference seismic modelling including surface topography, *Bull. Seism. Soc. Am.*, **91**, 1750–1764.

Israeli, M. and Orszag, S. A. (1981): Approximation of radiation boundary conditions, *J. Comp. Phys.*, **41**, 115–135.

Jastram, C., and Tessmer, E. (1994): Elastic modelling on a grid with vertically varying spacing, *Geophys. Prospect.*, **42**, 357–370.

Kristek, J., P. Moczo, and R.J. Archuleta (2002): Efficient methods to simulate planar free surface in the 3D 4th order staggered grid finite difference scheme, *Stud. Geophys. Geod.*, **46**, 355–381.

Kumar, S. and Narayan, J. P. (2008): Implementation of absorbing boundary conditions in a 4th order accurate SH-wave staggered grid finite difference algorithm with variable the size of a grid cell, *Acta Geophys.*, **56**, 1090–1108.

Levander, A. R. (1988): Fourth-order finite difference P-SV seismograms, *Geophysics*, **53**, 1425–1436.

Luo, Y. and Schuster, G. (1990): Parsimonious staggered grid finite differencing of the wave equation, *Geophy. Res. Lett.*, **17**, 155–158.

Madariaga, R. (1976): Dynamics of an expanding circular fault, *Bull. Seism. Soc. Am.*, **66**, 163–182.

Miyatake, T. (1980): Numerical simulation of earthquake source process by a three-dimensional crack model, Part I: Rupture process, *J. Phys. Earth*, **28**, 565–598.

Moczo, P., Labak, P., Kristek, J. and Franta, H. (1996): Amplification and differential motion due to an antiplane 2D resonance in the sediment valleys embedded in a layer over the half-space, *Bull. Seism. Soc. Am.*, **86**, 1434–1446.

Moczo, P. (1989): Finite difference technique for SH-waves in 2-D media using irregular grids- Application to the seismic response problem, *Geophys. J. Int.*, **99**, 321–329.

Moczo, P., Kristek, J. and Bystricky, E. (2000): Stability and grid dispersion of the P-SV 4th order staggered grid finite difference scheme, *Stud. Geophys. Geod.*, **44**, 381–402.

Moczo, P., Kristek, J., Vavrycuk, V., Archuleta, R. J. and Halada, L. (2002): 3D heterogeneous staggered-grid finite-difference modelling of seismic motion with volume harmonic and arithmetic averaging of elastic moduli and densities, *Bull. Seism. Soc. Am.*, **92**, 3042–3066.

Narayan, J.P. (2001a): Site specific strong ground motion prediction using 2.5-D modelling, *Geophys. J. Int.*, **146**, 269–281.

Narayan, J. P. (2001b): Site specific ground motion prediction using 3-D modelling, *ISET J. Earthq. Techn.*, **38**, 17–29.

Narayan, J. P. (2005): Study of basin-edge effects on the ground motion characteristics using 2.5-D Modeling, *Pure Appl. Geophys*, **162**, 273–289.

Narayan, J. P., and Ram, A. (2006): Study of effects of underground ridge on the ground motion characteristics, *Geophys. J. Int.*, **165**, 180–196.

Narayan, J. P., and Singh, S.P. (2006): Effects of soil layering on the characteristics of basin-edge induced surface waves and differential ground motion, *J. Earthq. Eng.,* **10**, 595–616.

Narayan, J. P. and Kumar, S. (2008): A 4th order accurate SH-wave staggered grid finite difference algorithm with variable the size of a grid cell and VGR-stress imaging technique, *Pure Appl. Geophys.*, **165**, 271–294.

Ohminato, T. and Chouet, B. A. (1997): A free surface boundary condition for including 3-D topography in the finite difference method, *Bull. Seism. Soc. Am.*, **87**, 494–515.

Oprsal, I. and Zahradnik, J. (1999): Elastic finite difference method for irregular grids, *Geophysics,* **64**, 240–250.

Oprsal, I. and Zahradnik, J. (2002): Three-dimensional finite difference method and hybrid modeling of earthquake ground motion, *J. Geophys. Res.*, **107** (B8), ESE 2–1 – ESE 2–15.

Pitarka, A. (1999): 3-D elastic finite difference modelling of seismic motion using staggered grids with variable spacing, *Bull. Seism. Soc. Am.*, **89**, 54–68.

Rodrigues, D. (1993) Large scale modelling of seismic wave propagation, Ph.D. thesis, École Centrale Paris, 112 pp.

Virieux, J. (1984): SH wave propagation in heterogeneous media, velocity stress finite-difference method, *Geophysics*, **49**, 1933–1957.

Virieux, J. (1986): P-SV wave propagation in heterogeneous media, velocity stress finite-difference method, *Geophysics*, **51**, 889–901.

Wang, Y., Xu, J., and Schuster, G.T. (2001): Viscoelastic wave simulation in basin by a variable-grid finite difference method, *Bull. Seism. Soc. Am.*, **91**, 1741–1749.

Zahradnik, J. P., Moczo, P. and Hron, F. (1993): Testing four elastic finite difference schemes for behaviour at discontinuities, *Bull. Seism. Soc. Am.*, **83**, 107–129.

SAŽETAK

P-SV valni algoritam konačnih razlika četvrtog reda točnosti na razmaknutoj mreži s varijabilnom veličinom mreže i VGR-metodom dijagnostike napetosti

J. P. Narayan i Sanjay Kumar

Prikazana je primjena VGR-metode dijagnostike napetosti (engl. *VGR-stress imaging technique*), kao slobodnog rubnog uvjeta na površini, u (2,4) P-SV valnom algoritmu konačnih razlika (engl. *finite difference*, FD) na razmaknutoj mreži s varijabilnom

veličinom mrežne ćelije. VGR je akronim za smanjenje vertikalne veličine mreže (engl. *vertical grid-size reductio*n). Kvalitativni i kvantitativni rezultati potvrdili su da efektivna debljina (engl. *effective thickness*, ETH) prvog sloja tla postaje za polovinu vertikalnog koraka mreže manja od pridijeljene debljine (engl. *assigned thickness*, ATH), ukoliko se metoda dijagnostike napetosti koristi kao slobodan rubni uvjet na površini. Rezultati različitih numeričkih eksperimenata otkrili su da uobičajeno korištena metoda dijagnostike naprezanja dovodi do značajne numeričke disperzije Rayleighevih valova, dok je VGR-metoda dovoljno učinkovita da to izbjegne. Nadmoć VGR-metode nad dobro poznatom metodom dijagnostike napetosti se stoga očituje u izbjegavanju značajne numeričke disperzije Rayleighevih valova u homogenom sredstvu, kao i manjem odstupanju u debljini sloja tla. Maksimalni omjer koraka mreže (tj. omjer najveće prema najmanjoj veličini mrežne ćelije) do 6.0 nije utjecao na točnost FD algoritma s varijabilnom veličinom mrežne ćelije. U slučaju varijabilne mreže, računalna memorija i vrijeme računanja potrebni za određeni model ruba bazena bili su 6.43, odnosno 16.62 puta manji nego u slučaju jednolike mreže.

Ključne riječi: valni algoritam konačnih razlika, četvrti red točnosti u prostoru, maksimalni omjer koraka mreže, VGR-metoda dijagnostike napetosti, stabilnost i disperzija mreže (numerička disperzija)

Corresponding author's address: J. P. Narayan, Department of Earthquake Engineering, Indian Institute of Technology Roorkee, Roorkee-247667, India, email: jaypnfeq@iitr.ernet.in